

7

Advanced Permanent Magnetic Materials

Felix Jimenez-Villacorta^{1,2*} and Laura H. Lewis²

¹Materials Science Institute of Madrid (ICMM-CSIC), 28049-Madrid, Spain

²Department of Chemical Engineering, Northeastern University, Boston, MA-02115, USA

*Corresponding author

Outline:

Introduction.....	161
Permanent Magnets: An Introduction.....	161
<i>Background: Permanent Magnet Uses and Metrics.....</i>	161
<i>Factors influencing the permanent magnet response.....</i>	164
<i>Advanced permanent magnets: nanostructuring strategy.....</i>	173
Nanostructured Permanent Magnetic Materials.....	174
<i>High-anisotropy nanocrystalline magnets.....</i>	174
<i>Alnico: the first nanostructured permanent magnet.....</i>	176
<i>Exchange-spring Magnets.....</i>	179
<i>Exchange-biased Magnets.....</i>	182
Concluding remarks.....	185
References	186

Introduction

Permanent, or hard, magnets deliver high magnetic flux combined with high stability against demagnetization. These properties render them essential in modern life: they are key components in efficient motors and electric machines and are integral in energy harvesting and conversion, power generation, sensors and in a plethora of automation-based devices. Permanent magnets are also highlighted as paradigmatic examples of the close relationship between basic research industry and technological implementation, as basic research advances may be directly transitioned to realization of better magnets with enhanced technical performance.

Throughout the 20th century, researchers have achieved advances (sometimes disruptive, sometimes just incremental) in diversification and improvement of candidates for numerous permanent magnetic applications. However, earlier researchers did not have the analytical probes and tools that are available today. In the last few years, recent insights derived from advanced tools, design of nanostructured magnets with controlled average crystallite size and orientation, optimized intergranular phase character and directed engineering of intrinsic features via atomic substitution will foster the realization of new materials that may be processed into the next generation of advanced permanent magnets.

This chapter is organized as follows: in the first section, concepts and tools utilized by researchers to develop, tailor and enhance the performance of permanent magnetic materials are presented; in the second section, an up-to-date report of materials synthesized and processed in diverse manners for development of the next generation of permanent magnets is described, with special attention devoted to technical achievements obtained on nanostructured magnets.

Permanent Magnets: An Introduction

Background: Permanent Magnet Uses and Metrics

Permanent magnets and their applications

Permanent magnets play a key role in modern life to enable the operation of numerous advanced devices and motors that facilitate the transformation of energy from one form to another. Their ability to maintain a large magnetic flux, even in the absence of an applied magnetizing field, or upon modifications of the environment (temperature, demagnetizing field, etc...) is a unique feature that can be employed in a wide variety of applications such as energy conversion and harvesting, power generation and transport, microwave communications, magnetic recording and sensor technologies. Basically, a permanent magnet is an energy-storage device; however, unlike other energy-storage devices such as batteries, its performance is not affected by repeated use, as it does not perform any net work on its surroundings. Such ability defines the possibilities and the potential applications in which a permanent magnet can be successfully employed.

Several approximations can be made to classify permanent magnets, from the physical effect produced (torque, linear force, induced electromotive force (emf), etc...) to the characteristic application (static or dynamic).[1] A list of common applications and appliances that incorporate permanent magnets illustrates their ubiquitous global presence (Table 7.1):

TABLE 7.1

A selection of applications utilizing advanced permanent magnets, like Nd₂Fe₁₄B (adapted from refs. [2,3])

Category	Application Examples
Computer and office automation	Hard disk drive and CD-ROM spindle motors Voice coil motors and pick-up motors Printer and fax motors
Consumer electronics	VCRs, cameras and DVD players Speakers, microphones and headsets Cell phones
Appliances	Household appliance motors and air conditioners Water pumps Security systems
Factory automation	Magnetic couplings and bearings Pumps Motors, servo motors and generators
Medical Industry	MRI equipment Surgical tools and medical Implants
Automotive & transportation	Starter motors and brushless DC motors Electric bicycles and hybrid/ electric vehicles Electric fuel pumps
Alternative Energy	Wind, wave, tidal power systems Power generation systems Energy storage systems
Military	Weapons systems, precision-guided munitions Vehicles, watercraft, avionics Communications systems, radar, satellites

A general classification scheme that identifies the dominant function of the magnet within a given class of application is provided below:

- Conversion of electrical energy to mechanical energy (motors, relays, loudspeakers, actuators, MEMS).
- Conversion of mechanical energy to electrical energy (generators, alternators).
- Use of magnetic attraction or repulsion to perform mechanical work (separators, bearing/coupling devices and torque drives).
- Guide and control electric charge, plasmas and electron or ion beams (cathode-ray tubes, klystrons, magnetrons, synchrotron insertion devices).
- Information storage (magnetic recording media) and detection capability (sensors, sensor “triggering”).

Units and figure of merit for permanent magnet strength

A permanent magnetic material is characterized by a broad and ideally square hysteresis loop that exhibits the dependence of the vector magnetization \vec{M} (usually in kA/m or emu/cm³), or the

magnetic flux density, \vec{B} (in Tesla) as a function of the applied magnetic field \vec{H} (in kA/m or Oe). Study of the second quadrant of the hysteresis loop (*i.e.*, the demagnetization curve) is essential, as the character of the magnet recorded in the second quadrant determines its suitability for a given application. In the case of permanent magnets, the figure of merit that defines their magnetic quality is the maximum energy product $(BH)_{max}$ (in kJ/m³ or MGOe), that is represented by the area of the largest rectangle that can be inserted in the second quadrant of the B - H loop, as depicted in Figure 7.1, indicating the total magnetic energy in the airgap. This quantity is an expression of the combination of the operative flux density (related to the most efficient magnetic induction) and the magnetomotive force (related to the resistance of a magnet to demagnetization, *i.e.*, the coercive force). Indeed, the development of permanent magnets during the last century has been motivated by the desire to achieve larger maximum energy products that can deliver energy transformation capability in small volume, thereby facilitating smaller and more efficient devices. For comparative purposes, common novelty magnets, such as so-called “refrigerator magnets”, possess a typical energy product of less than 8 kJ/m³ (<1 MGOe), whereas commercial advanced rare earth magnets possess values higher than 200 kJ/m³ (>25 MGOe).

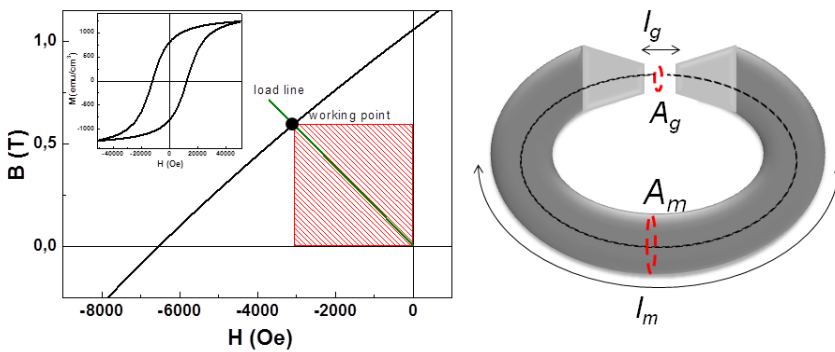


FIGURE 7.1

a) Plot of the 2nd quadrant of the B - H hysteresis loop that depicts the maximum energy product $(BH)_{max}$ rectangle, along with the load line and the working point (the load line intercepts the extrinsic demagnetizing curve at $(BH)_{max}$ only in conditions of maximum efficiency); b) illustration of an open magnetic circuit comprised of a permanent ring magnet, two soft magnetic ends to guide the magnetic flux and an empty airgap

The relevance of the maximum energy product as figure of merit may be illustrated as follows. The main function of a permanent magnet in an electric machine is to provide an external field in a magnetic circuit. The permanent magnet ring of length l_m provides a field of magnitude H_g within the air gap of length l_g , (represented in Fig. 7.1). The empty airgap is characterized by a demagnetizing field H_m and an associated magnetic flux B_m that exists between the two free poles. As known from classical electromagnetism, Ampère’s circuit law that relates magnetic fields to electric currents may be represented as $\oint Hdl = 0$, providing the condition below:

$$H_m l_m = H_g l_g \quad \text{Eq. [1]}$$

Assuming that the magnetic flux ϕ is fully contained in the ring magnet and thus the net magnetomotive force is zero, consideration of the flux path provides the relationship:

$$\phi = H_g A_g = B_g A_g = B_m A_m \quad \text{Eq. [2]}$$

Here, A_g and A_m are the cross sectional areas of the gap and of the magnet, respectively, and $H_g = B_g$ within the gap. In the general case that A_g and A_m are very different (typically $A_g \ll A_m$, since the flux lines that represent the magnetic field are confined by high-permeability soft magnetic ends framing the gap of the magnetic circuit) an expression of the gap field can be deduced from the two equations above:

$$H_g \sim \sqrt{\frac{V_m}{V_g} (B_m H_m)} \quad \text{Eq. [3]}$$

where $V_g = A_g l_g$ and $V_m = A_m l_m$. Thus the flux density (which is a measure of the energy stored in the air gap) is maximized when the product of $B_m \cdot H_m$ is optimum, allowing the maximum energy product $(B_m H_m)_{max}$ to quantitatively represent the performance capability of a permanent magnet. As such, $(BH)_{max}$ is a measure of the energy of the magnet in a magnetic circuit.

The load line or permeance coefficient, which represents the operating conditions of a given magnet, depends on the geometry and dimensions of the magnet and the gap (l_m/A_m), and may be determined at particular values of the magnetic flux and field.[4] The magnitude of the slope $\frac{B_m}{H_m}$ of this operating line is illustrated below:

$$\frac{B_m}{H_m} \sim \frac{A_g l_m}{A_m l_g} \quad \text{Eq. [4]}$$

The intersection between the second-quadrant demagnetization $B(H)$ curve and the load line is known as the working point of the magnet. For a fixed air gap, a particular $\frac{B_m}{H_m}$ slope where $B_m H_m$ is maximum is desirable (Fig. 7.1). Accurate knowledge of these quantities is important; the operation parameters must be far from vulnerability to demagnetization during the dynamic range of magnet operation [4,5].

The maximum energy product of a permanent magnet is determined by its “technical”, or extrinsic, magnetic properties as well as by its intrinsic properties. It may be optimized by tailoring structure-sensitive magnetic properties such as the residual magnetic flux (remanence, $B_R \equiv M_R$) and the resistance to demagnetization (coercivity, H_C), and/or by enhancement of fundamental intrinsic properties such as the saturation magnetization, M_S , the exchange interaction $J_{ex} \sim A_{ex}$, and the magnetocrystalline anisotropy energy, K . A brief overview of these magnetic features is presented to guide the reader to current pathways for the development of the next generation of permanent magnetic materials.

Factors influencing the permanent magnetic response

The quality of a magnet is determined by its magnetic properties. In turn, those magnetic properties are defined by the characteristic features of the material, *i.e.* composition, crystallinity and microstructure. The first two features, composition and crystallinity, determine the electronic structure of the constituent atoms and give shape to the atomic origin of intrinsic properties in magnetic materials. On the other hand, the microstructure dictates transference of the intrinsic

properties to the extrinsic properties, which describe the technical performance of these magnetic materials.

This section provides an overview of the magnetic properties of magnetic materials, and in particular of permanent magnets. First, the intrinsic parameters, accepted as the core of magnetic character, will be introduced. Later, definition of the extrinsic parameters will provide a context to describe technical magnetic performance and determine the dynamics of magnetic stability and reversal. Finally, an overview of the variety of magnetic anisotropy sources of both intrinsic and extrinsic origin that underlie the permanent magnet performance will be outlined.

Intrinsic parameters: M_s , A_{ex} , K

The fundamental properties of magnetic materials have atomic origins. These atomic features are as follows: the magnitude of the atomic magnetic moment, μ , that determines the saturation magnetization, M_s , per unit volume, ($M_s = |\sum \vec{\mu}|$, where μ is in $\text{A}\cdot\text{m}^2$ or J/T , M_s has units of kA/m , and $\mu_0 M_s$ is in T); the exchange interaction between atomic moments (J_{ex} or A_{ex} ; units are J/m) that couples electronic moments on distinct, often near-neighbor atoms; and the spatial arrangement of the magnetic atoms and their electronic orbitals within the crystal lattice that determines the magnetocrystalline anisotropy energy K , with units of J/m^3 . These intrinsic magnetic properties are thus determined by the crystal structure and composition of the material, and ideally insensitive to its microstructure, and form the basis of other critical parameters that quantify the magnetic response for engineering applications such as the Curie temperature, the exchange length and the domain wall width.

Within a bulk magnet the overall contribution to the atomic **magnetic moment** is given by the electron spin component of the total electronic angular momentum; the orbital component for $3d$ electrons is very small, with the electron orbital momentum quenched in many cases by the local crystal field.[6] On the other hand, $4f$ atoms possess a non-negligible orbital component. Also, the magnitude of the magnetic moment is decisively influenced by the localization or itinerancy character of the electrons, by virtue of electronic orbital broadening and hybridization. The magnetostatic energy, E_{mag} , which is the energy stored within a ferromagnet, may be defined as:[7]

$$E_{mag} = \frac{1}{2} N_d V \mu_0 M_s^2 \quad \text{Eq. [5]}$$

where N_d is the demagnetization factor which depends on the magnet shape, V is the volume and μ_0 is the magnetic permeability constant in free space.

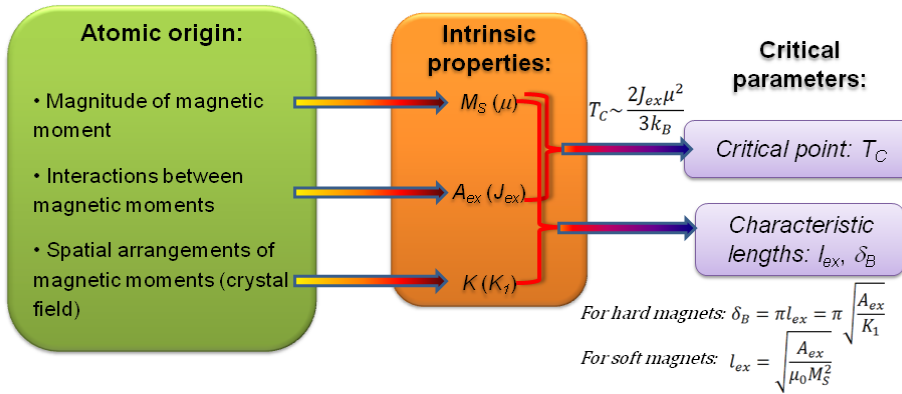


FIGURE 7.2

Depiction of relationships between the intrinsic properties of magnetic materials and parameters that quantify the magnetic response for engineering applications

The key descriptor of interatomic magnetic interactions is the quantum mechanical **exchange interaction**, E_{ex}^{ij} , which describes the expectation value of the energy between electrons i and j with overlapping wavefunctions. The exchange interaction is a consequence of the Pauli Exclusion Principle that describes the spin arrangement of electrons determined by their energy level, and is defined by the Heisenberg expression for a many-body system between neighboring atomic spins:

$$E_{ex}^{ij} = -2 \sum_{i,j} J_{ex} \vec{S}_i \vec{S}_j \tag{Eq. [6]}$$

where J_{ex} is the exchange integral. Ferromagnetic materials are characterized by a positive exchange coupling that causes the spin moments to be parallel. An analogous parameter is the **exchange stiffness A_{ex}** that is related to interatomic exchange strength and takes into account lattice symmetry considerations. For a cubic system:

$$A_{ex} = \frac{\Lambda}{a} J_{ex} S^2 \tag{Eq. [7]}$$

Here, a is the cubic lattice constant and Λ is the number of magnetic atoms in the unit cell. This parameter is often used in micromagnetic calculations and can be used to define long-range magnetic correlation. Spin fluctuations and vanishing of spontaneous magnetization are a consequence of competition between thermal energy ($\sim k_B T$) and exchange energy ($\sim JS^2$). The thermal energy overcomes the exchange energy at the Curie temperature, T_C , defined as the temperature transition from ferromagnetic to paramagnetic state:[7]

$$T_C \sim \frac{2J_{ex}\mu^2}{3k_B} \tag{Eq. [8]}$$

The scalar product contained within the simple Heisenberg expression (Eq. [8]) suggests that the exchange constant is an isotropic radial parameter that depends only upon the distance between magnetic moments. Extending beyond this simple approximation, the magnetic energy of ordered magnetic moments depends also on the relative orientation of such moments with respect to the crystal axes. This energy is the **magnetocrystalline anisotropy energy** that characterizes the

interaction between electrons and the crystalline electric field, with electron spin-orbit coupling donating an additional contribution. The magnetocrystalline anisotropy energy specifies the magnetic moment alignment along certain energetically-preferred orientations of the crystal (called the *easy axes*). Magnetic materials with technologically-useful permanent magnetic properties typically exhibit uniaxial crystal symmetry (usually adopting tetragonal, hexagonal or rhombohedral crystal structures, see Table 7.2).

The magnetocrystalline anisotropy energy, E_A , is approximated as a power series of the form:

$$E_A = \sum_n K_n \sin^{2n}(\theta) \quad \text{Eq. [9]}$$

where K_n is the uniaxial anisotropy constant for the n^{th} direction in the crystal and θ is the angle between the magnetization vector \vec{M} and the easy axis. In the case of strong uniaxial anisotropy, it is appropriate to utilize only the first term of the expansion, $E_A = K_1 \sin^2(\theta)$, where K_1 is the first anisotropy constant.

In the equilibrium state, a magnetic material tends to adopt the lowest possible magnetostatic energy configuration. Minimization of magnetostatic energy leads to the formation of magnetic domains, which are distinct regions of the material that exhibit uniform magnetic polarization. These regions of uniform magnetic polarization are separated by magnetization transitions known as *domain walls* with **domain wall energy** E_{DW} :

$$E_{DW} \approx 4 \sqrt{A_{ex} K_1} \quad \text{Eq. [10]}$$

TABLE 7.2

Intrinsic parameters of some representative hard magnetic materials (while they are not considered to be hard magnetic materials, Fe, Co and Ni were added for comparison purposes).

Material	$\mu_0 M_s$ (T)	T_c (K)	A_{12} ($\times 10^{-12}$ J/m)	K_1 ($\times 10^6$ J/m ³)	δ_B (nm)	l_{ex} (nm)	R_{sd} (nm)	Structure
Fe	2.15	1043	8.3	0.048	40	2.0	6	bcc
Co	1.76	1388	10.3	0.53	14	2.4	34	hcp
Ni	0.62	631	3.4	-0.0048	82	3.4	16	fcc
L1 ₀ -CoPt	1.00	840	10.0	4.9	4.5	3.5	310	Tetragonal
L1 ₀ -FePt	1.43	750	10.0	6.6	3.9			Tetragonal
L1 ₀ -FeNi	1.60	~750		1.3				Tetragonal
L1 ₀ -MnAl	0.75	650		1.7	15	4.8	90	Tetragonal
MnBi	0.78	630		1.2				Hexagonal
BaFe ₁₂ O ₁₉	0.48	723	6.3	0.33	14	5.9	290	Hexagonal
SrFe ₁₂ O ₁₉	0.47	733		0.35				Hexagonal
SmCo ₅	1.07	1003	22	17.0	3.6	4.9	425	Hexagonal
YCo ₅	1.06	987		5.5				Hexagonal
Sm ₂ Co ₁₇	1.30	1190	14	3.3	6.5**	3.3	250	Rhombohedral
Sm ₂ Fe ₁₇ N ₃	1.54	749	12	8.9	3.6**	2.5	190	Rhombohedral
Nd ₂ Fe ₁₄ B	1.61	585	7.7	5.0	3.9	1.9	107- 300	Tetragonal
Pr ₂ Fe ₁₄ B	1.41	565	12	5.6	4.6**		300	Tetragonal

** Domain wall width estimated from Eq. [11]

The characteristic length scale governing the thickness of the domain wall in hard magnetic materials with large magnetocrystalline anisotropy energies, is determined by competition between the exchange energy and the magnetic anisotropy energy. The anisotropy energy E_A favors a narrow domain wall width while the exchange energy E_{ex} favors smoother transitions between domains resulting in thicker domain walls [8]. The magnetic exchange length l_{ex} can be derived as the thickness of the transition regions between two opposite magnetic orientations* and is a key parameter that describes the magnetic coupling between grains that constitute a magnet; thus it is a critical parameter in dense-packed nanocrystalline materials. For a typical domain-wall type in a bulk magnet (Bloch type), the domain wall width, δ_B , can be estimated as:

$$\delta_B = \pi l_{ex} = \pi \sqrt{\frac{A_{ex}}{K_1}} \quad \text{Eq. [11]}$$

where the parameters are defined as previously.

Summarizing, intrinsic magnetic properties such as the saturation magnetization, the exchange interaction and the magnetocrystalline anisotropy determine the potential of a given magnetic material to exhibit superior permanent magnetic character. However, it is the microstructure of the magnet that determines whether these magnetic properties may be harnessed for outstanding permanent magnetic performance.

Extrinsic parameters: M_R , H_C

Extrinsic or “technical” magnetic parameters refer to those properties that are dependent upon the magnet microstructure. Microstructural features such as the size of the constituent grains and their relative alignment within the magnet are reflected in the hysteresis loop. Specifically, in an ideal permanent magnet, a large residual magnetic flux that exists at zero field (the “remanence” or B_R , in T) and a large resistance to demagnetization (the “coercivity” or H_C , in kA/m) must be preserved. Both parameters contribute to the squareness and broadening of a magnetization loop which directly impact the maximum energy product, $(BH)_{max}$. A compilation of extrinsic parameter values for a variety of permanent magnetic materials are provided in Table 7.3. In the idealized case of a rectangular M - H loop (that is, $M_R = M_S$ and $\mu_0 H_C = M_R/2$), the limit of the maximum energy product is determined as:

$$(BH)_{max} \leq \frac{1}{4} \mu_0 M_S^2 \quad \text{Eq. [12]}$$

Remanence is indicative of the amount magnetic flux existing at zero field, defining the magnetic field delivered by the magnet to the airgap. It depends on the vector sum of magnetic moments at such zero field. Assuming the simple Stoner-Wohlfarth model for single domain particles,[9] by which the magnetic reversal process in a magnetic particle system occurs through simple coherent reverse, a particle system with a random distribution of easy axes possesses an estimated

* Another characteristic exchange correlation length scale has been defined, mainly in soft magnetic materials where anisotropy is small, that determines the distance below which atomic exchange interactions dominate typical magnetostatic fields. In the limit of small anisotropy energy, the exchange length can be expressed as:

$$l_{ex} = \sqrt{\frac{A_{ex}}{\mu_0 M_S^2}}$$

remanent magnetization value which is half of the saturation magnetization, $M_R = M_S/2$. Larger M_R values can be reached with improved easy axis alignment, as well as with increasing magnetic intergranular interaction. This knowledge can be utilized for practical purposes in the realization of a permanent nanostructured magnet (mainly the first condition, since increasing magnetic intergranular interaction may render a collateral reduction of the coercivity).

TABLE 7.3

Extrinsic parameters of some representative permanent magnetic materials

Material	B_R (T)	$\mu_0 H_C$ (T)	$(BH)_{max}$ ($\times 10^3$ J/m ³)
Alnico (isotropic)	0.6-1.0	0.1-0.2	10-30
Alnico (anisotropic)	1.3-1.4	0.3-0.4	40-80
AFe₁₂O₁₉ (sintered)	0.39	0.3	28
SrFe₁₂O₁₉	0.2-0.4	0.13-0.37	10-40
SmCo₅ (metal-bonded)	0.92	1.88	175
SmCo₅ (polymer-bonded)	0.58	1.00	60
Sm₂Co₁₇/SmCo₅ (sintered)	1.08	1.0	225
Nd₂Fe₁₄B (sintered)	1.0-1.4	1-2.5	200-440
Nd₂Fe₁₄B (polymer bonded)	0.6-0.7	0.75-1.5	50-100
Nd₂Fe₁₄B/α-FeCo (nanocomposite)	1.4-1.6	1.0-1.8	320-480
L1₀-MnAl (alloy)	0.5-0.6	0.2-0.4	40-70
L1₀-MnAl (nanoparticles)	0.25-0.5	0.36-0.56	38
MnBi (nanostructured powder)	0.25	1.9-2.1	14
MnBi (bonded)	0.50	1.1 (300 K) 2.5 (540 K)	60
Zr₂Co₁₁ (isotropic ribbons)	0.6	0.2	42
Zr₂Co₁₁ (aligned nanoparticles)	0.84	0.44	132
HfCo₇ (isotropic ribbons)	0.7	0.2	35
HfCo₇ (aligned nanoparticles)	0.9	0.45	100

The magnetic coercive field is indicative of the magnetomotive force against which a magnet can operate, and thus it is of paramount importance where magnetic devices include large air gaps or are subjected to large demagnetizing forces. The physical origin of the coercivity is the magnetocrystalline anisotropy field, H_A , which sets an upper limit on the coercive field value that can be realized in a particular material. If magnetic reversal of the material occurs only through coherent rotation of the magnetic vector from one easy axis to another against the magnetocrystalline anisotropy (Stoner-Wohlfarth reversal), a maximum coercivity is realized which is given by:

$$H_C^{max} = H_A = \frac{2K_1 + 4K_2}{\mu_0 M_S} \quad \text{Eq. [13]}$$

In the case of strong uniaxial anisotropy ($K_1 \gg K_2$), Eq. [14] can be reduced to the expression:

$$H_C^{max} = H_A \approx 2K_1 / \mu_0 M_S \quad \text{Eq. [15]}$$

Magnetization reversal processes can be complex. Real values of coercive field are always lower than the corresponding anisotropy field H_A due to the extreme sensitivity of the magnetization

reversal process and formation of reverse domains to the microstructure of the magnet. As a first approximation, a phenomenological description of coercivity is provided by Kronmüller and co-workers, derived from the Brown-Aharoni model:[10,11,12,13]

$$H_C = \alpha H_A - N_{eff} M_S \quad \text{Eq. [14]}$$

where α and N_{eff} are microstructural parameters (α is defined in the range $0 \leq \alpha < 1$ and depends on defects and grain alignment, while N_{eff} is the effective demagnetization factor, stemming from macroscopic sample or the microscopic grains).

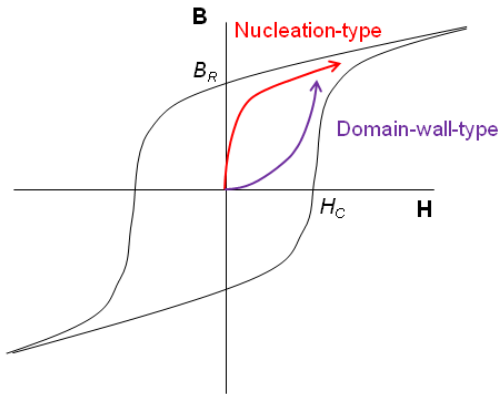


FIGURE 7.3

Schematic representation of virgin curves for nucleation-type and domain-wall-type magnets

The coercivity in a permanent magnet can encompass a rich variety of magnetization reversal processes (coherent rotation, nucleation, and domain wall pinning). However, depending on the type of magnet and its microstructure, one of these mechanisms can dominate the process. Under the action of an applied field, magnetization reversal can be controlled by nucleation of reverse domains or by pinning of domain walls. In nucleation-controlled magnets, the reversal field is controlled by the nucleation field, H_N , that is necessary to create a region of reverse polarization within the material. In the pinning-type magnets, structural and magnetic inhomogeneities in the microstructure impede domain wall motion. The characteristic feature that allows these two magnetization reversal mechanisms to be distinguished is their initial magnetization curve (see Fig. 7.3):[14] while magnetic saturation can be achieved quickly at relative low fields in nucleation-type magnets (for example, sintered $\text{Nd}_2\text{Fe}_{14}\text{B}$ magnets, where nucleation occurs at defects of the grains surface), a higher field is required to fully magnetize the material in pinning-type magnets (for example, Cu-doped $\text{Sm}_2\text{Co}_{17}$ magnets) [15,16].

The art of making a high-quality permanent magnet is to engineer a microstructure where the fully-polarized state (at saturation magnetization) is stabilized against the creation of reverse-polarization domains: either reverse domains are difficult to nucleate, or domain walls are strongly pinned and cannot move easily to expand areas with reversed magnetization. In both cases, control of coercivity implies control of the microstructure at the nanoscale, and thus nanoscopic tailoring is of paramount importance for the design of next-generation permanent magnetic materials.

Sources of magnetic anisotropy

One aspect of magnet performance is the coercive field which is limited by the magnetocrystalline anisotropy. Higher anisotropy is reflective of a larger energy difference between magnetization aligned in a preferred orientation (easy axis) and the hard direction. However, it is possible to donate anisotropy through other mechanisms, as depicted in Fig. 7.4.

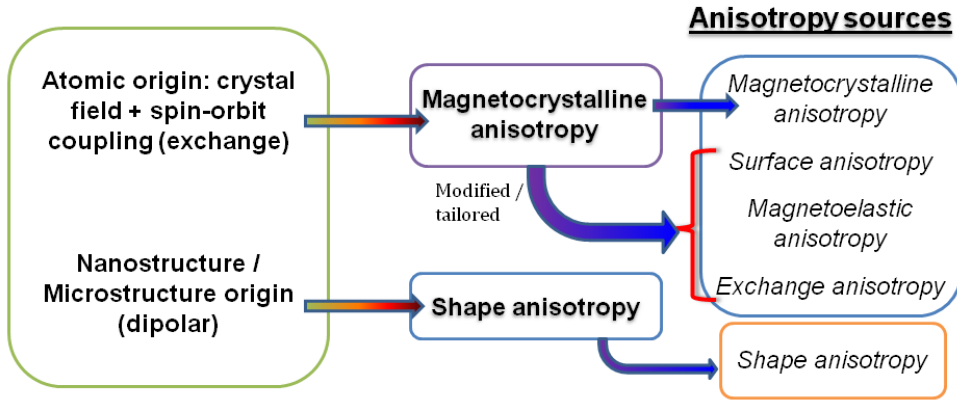


FIGURE 7.4
Schematic representation of the magnetic anisotropy sources and their origin

Of relevance to nanoscaled permanent magnet systems, Néel predicted that the anisotropy energy density will be modified significantly if the dimensions of magnetic particles are comparable to the magnetic exchange length l_{ex} in the nanometer range. Atoms residing on the surface of nanoparticles can provide a unique contribution to the anisotropy energy since the local symmetry of these atoms is different from that of the bulk. The lowered symmetry at the surface strongly modifies the magnetocrystalline contribution, thereby yielding a so-called **surface anisotropy**, K_s . This surface anisotropy is usually considered in nanoparticle and thin film systems and augments the volume magnetocrystalline anisotropy energy K_1 to provide an overall anisotropy energy K as:

$$K \approx K_1 + 2K_s/t \tag{Eq. [15]}$$

where t is the thickness of the film (or the particle dimensions).

The spin-orbit interaction, in conjunction with the overlap of wave functions between neighboring atoms, is also responsible for **the magnetoelastic anisotropy** that may be induced in a strained system. Strain effects are frequently found in intergranular or interphase interfacial regions, often due to lattice mismatch between their constituent materials. The crystal field can be modified by strain in a ferromagnetic material of nanoscale dimensions, resulting in alteration of the magnetocrystalline anisotropy and of the easy axis of magnetization. The magnetoelastic anisotropy energy K_{me} may be represented as

$$K_{me} = \frac{3}{2} \lambda_m \sigma \cos^2 \theta \tag{Eq. [16]}$$

where $\sigma = \varepsilon E$ the stress coefficient (ε is the strain coefficient and E is the elastic modulus), λ_m is the magnetostriction constant and θ is the angle between magnetization and the direction of uniform stress (typically parallel to the interface plane between two phases).

Another source of anisotropy that also has its origins in the nature of the interface is the **exchange anisotropy** that is derived from strong exchange coupling between the magnetic moments of an antiferromagnetic (AF) phase and those of a ferromagnetic (FM) component. The effects of exchange anisotropy are clearly visible in the hysteresis loop as a lateral shift, or exchange bias H_E , in the field axis that is manifest as in increased coercivity. Using a simple coherent reversal model to describe the FM/AF exchange coupling at the interface, the exchange anisotropy energy K_{eb} may be estimated as:

$$K_{eb} \sim H_E M_S \quad \text{Eq. [17]}$$

dependent also on the dimensions of the FM phase. While previously-described anisotropy sources are uniaxial, *i.e.*, feature an easy axis, exchange anisotropy is unidirectional.

These additional sources of magnetic anisotropy (magnetoelastic, surface, exchange) all intrinsically have an atomically-localized nature, determined by crystallographic orientations or atomic-length interfacial exchange. A rather different form of magnetic anisotropy, determined by the geometric shape of a magnetic body, is **shape anisotropy**.

The origin of this shape anisotropy resides in the demagnetization field that is created in the surface poles of a magnetized material. As a first approximation, this demagnetization field can be defined as:

$$\vec{H}_d = -N_d \vec{M} \quad \text{Eq. [18]}$$

where N_d is the demagnetizing factor (tensor) in the direction of \vec{M} , appropriate to the particular shape of the body. Every axis has its own demagnetizing factor, related one each other through the expression $N_x + N_y + N_z = 1$ ($=4\pi$ in the CGS). Under the situation of a fully magnetized ellipsoidal particle with z as the long (*i.e.*, easy) axis) and x and y dimensions defining the short axes (thus $N_x=N_y$), the shape anisotropy energy K_d can be expressed as:

$$K_d = -\frac{1}{2} \mu_0 M_S^2 [N_x - N_z] \cos^2 \theta \quad \text{Eq. [19]}$$

where θ is the angle between the easy axis and the magnetization. In an acicular ellipsoid with a very long axis (*i.e.* $z \gg x$), $N_z \rightarrow 0$ whereas $N_x \rightarrow 1/2$. Also, in the spherical case, $N_x=N_y=N_z = 1/3$, and no shape anisotropy will be observed.

All these anisotropies can be employed in new strategies for development of advanced permanent magnetic materials. To this end, nanostructuring is a powerful route to engineer nanostructured permanent magnetic materials as it allows tailoring of both the local anisotropy (the generation of magnetoelastic, surface or exchange anisotropy contributions manifest in grain boundaries, interphase interfaces and surfaces), and of the nanostructural configuration (for the development and optimization of shape anisotropy, as well as for averaging of the local anisotropy terms).

Advanced permanent magnets: nanostructuring strategy

Successful remanence and coercivity optimization in permanent magnet materials requires the control and manipulation of magnetic anisotropy and crystallographic alignment. The magnetic anisotropy may be developed using domain wall pinning, magnetocrystalline anisotropy, surface and magnetoelastic anisotropies, shape anisotropy and exchange anisotropy, preferably in combination of two or more of them, rendering a high coercivity H_c to foster a high energy product, $(BH)_{max}$.

Potential strategies to control and enhance the hard magnetic properties of a magnetic material would comprise tailoring the composition, the crystal structure and the microstructure. By employing composition and crystal structure optimization, intrinsic magnetic properties can be manipulated, including pathways to control magnetization, exchange and magnetocrystalline anisotropy. Doping compounds with magnetic $3d$ -atoms (to increase the magnetization) or with heavy atoms (to increase the magnetocrystalline anisotropy) remain standard routes for optimization of magnetic properties. [17,18]

On the other hand, control of the microstructure (grain size, texture, etc.) can allow manipulation of extrinsic features using diverse methods to design characteristic lengths of the magnetic phase(s). *A priori*, there are many advantages in nanostructuring a magnetic material.[19] While large magnetic entities, such as micron-sized grains, tend to reverse via nucleation of reverse magnetic regions that form domain walls, nanoparticle systems cannot tolerate the formation of domain walls as it is a high-energy process. In this case magnetic reversal occurs through coherent rotation of magnetic moments, with a subsequent increase of the coercivity H_c that may approach the large values of the anisotropy field H_A . The critical particle diameter that separates reversal by domain wall nucleation from reversal by coherent rotation may be estimated by examination of the energy increase to the system through formation of a domain wall. In the case of a spherical particle of volume V_{sphere} , competition between the gain of magnetostatic energy ($\approx \frac{\mu_0 M_S^2}{12} V_{sphere}$) and the formation of a domain wall (energy for two hemispherical domains is $\approx 4\sqrt{A_{ex}K_1}S_{sphere}$) yields a critical single-domain radius, R_{sd} , as provided below:

$$R_{sd} \sim \frac{36\sqrt{A_{ex}K_1}}{\mu_0 M_S^2} \quad \text{Eq. [20]}$$

The coercivity enhancement achieved by creating isolated magnetic domains with the critical single-domain radius is a compelling motivation for nanostructural engineering. In fact, for selected hard magnetic phases the critical radius R_{sd} can be quite large ($R_{sd} > 100$ nm, Table 7.2). Extending the idea of magnetic coupling, an active to the optimization of magnetic properties is to develop magnetic nanocomposite materials, where two or more magnetic phases combine at the nanoscale to create a material with magnetic properties that are superior to those of either phase alone. An in-depth exposition of the synthesis, processing and performance of permanent magnetic nanocomposites (also known as exchange spring or exchange bias nanostructured materials) is provided in the next section.

An interesting route to high energy-product permanent magnets is to utilize nanostructuring to stabilize metastable or new crystal structures. Examples of nanoparticle cobalt-based systems (CoC_x , YCo_5 , HfCo_7) which display large values of coercivity and maximum energy product were recently reported.[20,21,22] Another example involving the positive effects of nanostructuring on the synthesis of hard magnetic materials was observed with the L1_0 -MnAl intermetallic alloy. This tetragonal phase is typically achieved from a metastable high-temperature precursor ε -MnAl after

annealing processes at moderate temperatures ($T_{ann} \sim 700-900$ K).[23,24,25] However, significant reduction of the phase transformation temperature (to about $T \sim 550-600$ K) is reported in nanostructured MnAl,[26,27] providing an attractive low energy route for the fabrication of permanent magnets.

The realization of bulk advanced permanent magnets obtained from non-equilibrium synthesis and processing techniques is an extraordinarily difficult challenge, requiring dedicated and synergic interdisciplinary research carried out by experienced teams of metallurgists, computational experts, solid state researchers, nanoscientists and materials engineers. Rapid solidification methods,[25,28] ball milling,[29,30] electrospinning,[31,32] cluster-gun deposition[20] and other fabrication methods that can produce metastable phases are ideal tools to attain the desirable high-coercivity nanocrystalline structures. In the latter part of this Chapter, a broader overview of the fundamentals and recent investigations on magnetic nanostructured materials with permanent magnetic properties is provided.

Nanostructured Permanent Magnetic Materials

Pioneering efforts to develop permanent magnetic materials have focused on control and tailoring of intrinsic and extrinsic magnetic properties, including optimization of composition, crystalline structure and microstructure. In this section, a survey is provided of different approaches that have been employed in the quest for advanced permanent magnets. After an introduction of various high-coercivity magnetic phases, attention will be directed on the development of multiphase nanocomposites that is inaugurated with a brief description of the first nanostructured permanent magnet, the family of Alnico magnets. Finally, recent efforts to engineer superior magnetic response in exchange-coupled nanocomposite materials will be reviewed. Promising candidates for next-generation permanent magnets will be introduced, including exchange-bias permanent magnets comprised of ferromagnetic and antiferromagnetic nanophases. These examples represent promising pathways for creation of new permanent magnetic materials for an immense variety of advanced technological applications.

High-anisotropy nanocrystalline magnets

Magnetic features of high-anisotropy magnets

The first milestone in the rational design of intrinsic properties (magnetocrystalline anisotropy) for permanent magnet behavior was achieved in the development of the ceramic hexaferrites.[33] These magnetic iron-oxide compounds, with composition of the type $MO \cdot 6Fe_2O_3$ ($MFe_{12}O_{19}$), where M represents the divalent metals Ba, Sr or Pb, exhibit $(BH)_{max}$ values of $15-65$ kJ/m³ ($\sim 2-8$ MGOe) and outstanding technical advantages as they are inexpensive, chemically inert and easy to process. Moreover, these oxide magnets exhibit relatively high Curie temperatures ($T_c \sim 950$ K), with outstanding performance at high temperatures. It is no surprise that this family of magnets dominate the permanent magnet market at the present, with $\sim 80\%$ of the total production.[14]

More than a decade after the introduction of ferrite magnets into technological application, the discovery of rare earth – transition metal (RE-TM) intermetallic compounds represented a leap in the magnetic performance of permanent magnets. Ferromagnetic RE-TM intermetallic phases of the hexagonal $CaCu_5$ -type crystal structure (space group $P6/mmm$) $RE-Co_5$ (RE = Y, Ce, Pr, Sm), exhibited high maximum energy products close to 140 kJ/m³ (18 MGOe) in part due to the

extremely high anisotropy energy, donated by the rare-earth component.[34] Continued exploration of the RE-TM alloys in the 1970's and 1980's focused on substitution of one RE atom in Ca sites of the structure by a pair ("dumbbell") of Co atoms, with the purpose of increasing the total magnetization (and hence the magnetic flux) without a significant reduction of magnetocrystalline anisotropy. In this manner the SmCo-based family of magnets was realized: the "2-17" compound (through substitution of 1 RE element by 1 pair of Co atoms every 3 unit formula), the "1-12" compound (through substitution of 1 RE element by 1 pair of Co atoms every 2 unit formula), the "3-29" compound (through substitution of 2 RE by transition metal pairs every 5 unit cells, or equivalently alternate stacking of "2-17" and "1-12" cells), and finally the "1-7" compound, with variable replacement of RE atoms by dumbbell pairs of Co atoms (Co:RE compositional range from Co:RE = 5 to 8.5).[35,36]

The record $(BH)_{max}$ values displayed by the RE-TM family of magnets was obtained with discovery of $Nd_2Fe_{14}B$ magnets (simultaneously developed by Sumitomo Special Metals Co., General Motors, and the U.S. Naval Research Laboratory).[28,37] The $Nd_2Fe_{14}B$ compound displays a complex tetragonal crystal structure (space group $P4_2/mnm$) with 68 atoms and six distinct iron sites per unit cell (see Fig. 7.4).[38] Record energy products were obtained with subsequent optimization of composition and post-solidification processing, with values up to 400 kJ/m^3 ($\sim 50 \text{ MGOe}$), remanences $B_R \sim 1.4 \text{ T}$ and typical intrinsic coercivities $H_C \sim 8000\text{-}16000 \text{ kA/m}$ ($10\text{-}20 \text{ kOe}$). Some drawbacks of this intermetallic compound is its relatively low Curie temperature ($T_C \sim 600 \text{ K}$, with operating temperatures typically restricted to 400 K), its brittleness and a large propensity for corrosion.[38,39]

Recent developments in high-anisotropy nanocrystalline magnets

Recent efforts to optimize the microstructure and the composition of RE-TM magnets have led to incremental advances in the performance of the "already effective" rare earth magnets. For Sm-based magnets, incorporation of interstitial N result in the stabilization of the $Sm_2Fe_{17}N_3$ phase, with predicted energy products of up to 470 kJ/m^3 (59 MGOe),[40] although experimental values only reach $\sim 160 \text{ kJ/m}^3$ ($\sim 20 \text{ MGOe}$).[39] On the other hand, Nd-based magnets have improved their high temperature performance with the addition of Dy traces.[39]

Creating a high-quality nanostructured hard magnetic material can be a challenge. Rapid solidification methods, ball milling, electrospinning, and cluster-gun deposition and other fabrication methods that can produce metastable phases are ideal tools to attain the desirable high-coercivity nanocrystalline structures [41,42]. Co-based nanowires, synthesized using self-assembled anodic alumina templates and displaying combined magnetocrystalline and shape anisotropies, are being studied for potential applications as permanent magnets.[43] Rapid solidification by melt spinning creates nanostructured flakes that can be processed into dense magnets. The alternative method of electrospinning was recently applied to achieve $SrFe_{12}O_{19}$ ferrite nanofibers [31,32]. Recently, researchers have tried to synthesize nanoparticles of Sm-based and Nd-based magnets by surface-assisted ball milling [44,45] for use, in many cases, in the synthesis of nanocomposite magnets (see Subsection 2.3). Also, when the grain size descends to the nanoscale, quantum-mechanical exchange becomes important as spins at the peripheries of neighboring nanograins become strongly exchange-coupled [46].

Price volatility of rare-earth elements is promoting reinvigorated research on rare-earth-free permanent magnetic materials. In many cases, potential hard magnetic candidates with high magnetocrystalline anisotropy were already known, and are being revisited in efforts to tailor their magnetic properties with increased accuracy and efficiency. The current list of alternatives

materials systems to rare-earth magnets comprises uniaxial intermetallic compounds (mainly with tetragonal and hexagonal crystal structures) such as $L1_0$ magnetic compounds [47] ($L1_0$ -FeNi, $L1_0$ -MnAl; also $L1_0$ -CoPt and $L1_0$ -FePt, but for cost reasons these compounds are disregarded for fabrication of bulk magnets), the ordered interstitially-modified compound α'' -Fe₁₆N₂ and MnBi [29,48]. Promising developments have been reported in the last few years, and precise tailoring of their magnetic features are pursued following both atomic-scale (intrinsic) and nanoscale (extrinsic) synthesis and processing strategies.

Alnico: the first nanostructured permanent magnet

Magnetic features of Alnico magnets

The development of Alnico magnets may be considered as the first example of tailoring extrinsic magnetic properties through manipulation of the microstructure. This family of magnets constitutes an important milestone in the trajectory of technologically-important magnetic materials that occurred simultaneously with the beginnings of materials science as an established field of study. Study of the optimization history of these pioneering magnetic alloys provides illumination concerning current and future pathways to realize new permanent magnetic materials, in particular with realization and optimization of nanocomposite magnets.

Iron and its ferromagnetic alloys are ideal starting materials for advanced permanent magnets: the Fe-Co alloys possess the largest magnetic moment ($\sim 2.5 \mu_B$ /atom) among the transition metal alloys, also exhibiting high Curie temperatures ($T_c \sim 1200$ K).[7] However, the high-symmetry body-centered cubic (*bcc*) crystal structure of α -FeCo results in an intrinsically low magnetocrystalline anisotropy energy, with a measured coercivity of only a few oersteds. Larger coercivities can be generated in iron-based alloys by the introduction of non-magnetic inclusions (inclusion-hardened magnet steels) to pin magnetic domain walls in the material, displaying maximum coercivities in the range of a few hundred Oersteds.[49]

Building on this information, composite Alnico magnets were developed with Fe, Co, Ni and Al as the main constituents. Alnico magnets were once the most widely-used family of permanent magnet materials, following the discovery by Mishima in Japan (1931)[50] that an alloy containing 58 wt.% Fe, 30% Ni and 12% Al had a coercivity of 400 Oe, nearly double that of the best magnetic steel.[7] Several decades later the Alnico family was largely replaced by hard magnetic hexaferrites and rare earth-transition metal alloys, with major applications confined to beam focusing, sensors, speakers and pick-ups.[51] However, Alnico magnets still play an important role in the pool of permanent magnetic materials, thanks to their large saturation magnetization in the range of 2 T. Moreover, due to current strategic materials supply issues,[52] this family of magnets have received renewed attention.[53]

Analogue to the Fe-Ni-Al ternary phase diagram,[54] the Alnico system displays a miscibility gap in the solid state; below a critical temperature in the vicinity of 1140 K (~ 865 °C, Fig. 7.5) a homogeneous *bcc* Fe-Co-Ni-Al parent phase spinodally decomposes into two phases: a ferromagnetic FeCo-rich phase and a weakly-magnetic NiAl-rich phase. These two phases both possess a *bcc* crystal structure with slight differences in the cubic lattice parameter. The phase decomposition occurs readily at elevated temperature and the resultant microstructure develops by a gradual fluctuation and periodicity in composition that is different from typical nucleation and growth processes.[55]

Alnico magnets tend to be hard and brittle and are manufactured by a cast or sintering process.[56] The cast alloys have very coarse grains, of the order of 1 mm, while the sintered alloys are finer

grained and mechanically stronger, with better surface finish, but somewhat inferior properties. Since the permanent magnetic properties of as-cast and as-sintered Alnico are poor, a special three-stage heat treatment is necessary to produce the target nanocomposite structure with optimized magnetic properties (see Figure 7.5):[57,58,59]

1. Heating to ~ 1550 K for homogenization.
2. Slow cooling ($\sim 1\text{-}5$ K/s) with or without an aligning magnetic field to about 800-1100 K
3. Tempering-ageing at ~ 900 K for several hours to develop the desired microstructure.

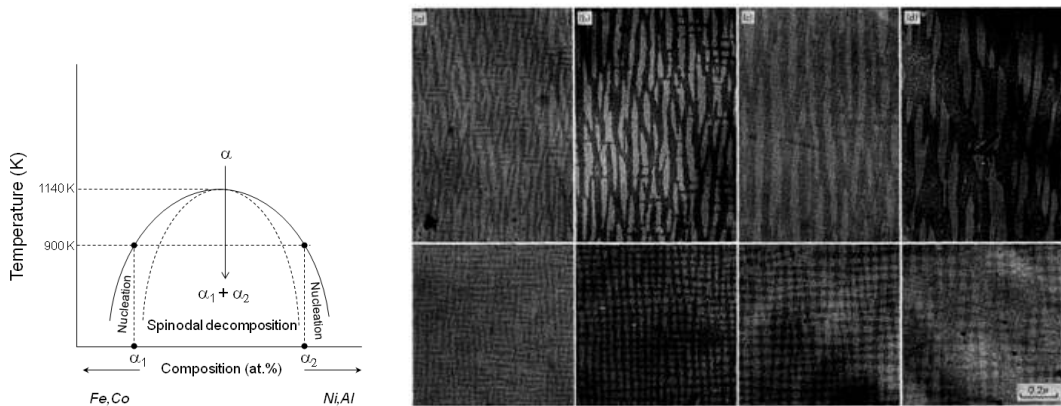


FIGURE 7.5

Schematic phase diagram depiction showing the spinodal decomposition of Alnico alloys (the two bcc phases α_1 and α_2 , FeCo-rich and NiAl-rich, respectively, stem from the parent bcc phase, α). Electron micrographs of Alnico 8 specimens annealed under an applied field at several temperatures (from Ref. [57]). Reprinted with permission from The Japan Institute of Metals and Materials). The upper and lower rows correspond to the surface parallel and perpendicular to the field, respectively

The magnetic characteristics of a selection of grades of cast Alnico magnets are summarized in Table 7.3. The application of a magnetic field (250 – 1500 Oe) during the annealing process produces an anisotropic nanostructure containing elongated FeCo precipitates aligned parallel to the direction of the magnetic field.[57,60] Application of stronger magnetic fields cause the rods to form preferentially along the (100) direction,[60] introducing an important shape anisotropy that raises the maximum coercivity to ~ 2 kOe and providing an enhanced remanence to yield an improved maximum energy product to the range of 40–80 kJ/m³ ($\sim 5\text{-}10$ MGOe).[61]

TABLE 7.4

Magnetic properties of some representative cast Alnico alloys (from Refs. 55, 62 and 63)

	Alloy Designation	Approximate composition of alloy (Balance Fe for all alloys)	B_R (T) [M_R/M_S]	H_c (kA/m) [Oe]	$(BH)_{max}$ (kJ/m ³) [MGOe]	T_c (°C)	Packing fraction (ρ)
Isotropic	Alnico 1	Co(5%)Ni(20%)Al(12%)	0.71 [0.69]	38 [480]	11.1 [1.4]	760	0.48
	Alnico 2	Co(13%)Ni(17-19%)Al(10%)Cu(3-6%)	0.71-0.78 [0.70]	46 [540-580]	13.5 [1.7]	800-815	0.51
	Alnico 3	Ni(25%)Al(12%)Cu(0-3%)	0.63-0.70 [0.47]	45 [570]	10.7 [1.4]	740-760	0.47
	Alnico 4	Co(5%)Ni(27-28%)Al(12%)	0.52-0.55 [0.59]	57 [720]	11.1 [1.4]	760	0.41
Anisotropic	Alnico 5	Co(24%)Ni(14%)Al(8%)Cu(3%)	1.28	51 [640]	43.8 [5.5]	890	0.57
	Alnico 5 DG	Co(24%)Ni(14%)Al(8%)Cu(3%)	1.28-1.33 [0.94]	53 [575-640]	57.7 [6.5]	860	0.57
	Alnico 5-7	Co(24%)Ni(14%)Al(8%)Cu(3%)	1.35 [0.97]	59 [740]	59.7 [7.5]	890	0.60
	Alnico 6	Co(24%)Ni(16%)Al(8%)Cu(3%)Ti(1%)	1.05 [0.89]	62 [780]	31.0 [3.9]	860	0.50
	Alnico 8	Co(35%)Ni(15%)Al(7%)Cu(4%)Ti(5%)	0.82	148 [1860]	42.2 [5.3]	860	0.30
	Alnico 9	Co(35%)Ni(15%)Al(7%)Cu(4%)Ti(5%)	1.06	119 [1500]	71.6-73.6 [9.0-9.2]	860	0.50
	Columax (Nb 1%)	Co(25%)Ni(13%)Al(8%)Cu(3%)Nb(1%)	1.35 [0.975]	59 [740-840]	60-69 [7.5-8.6]	860	0.61

Recent Alnico developments

Over the course of their development, refinement of the nanostructure and composition have been pursued to enhance the magnetic performance of the Alnico alloys. For instance, it is known that cobalt and copper additions lower the transformation temperature.[7] Cobalt also increases the Curie temperature, facilitating also the field-assisted texture development during aging. The relative volume of the FeCo-rich precipitates in the alloy is a key parameter that provides a remanence enrichment at the expense of coercivity reduction; a balance of these two effects yields an optimized FeCo nanoprecipitate volume fraction that is around 50-60% of the total volume.[62] Recent investigations in the Alnico family of alloys have employed modern tools such as high-resolution electron microscopy to characterize nanoscale and interphase interfacial properties; apart from quantitative correlations between the elongated microstructure and crystallographic orientation, high-resolution composition characterization has revealed that fluctuations in Co content in the final product are less abrupt compared with the spinodal compositional oscillations of Fe.[64] Magnetic microprobe techniques have confirmed the existence of a complex magnetic structure in anisotropic Alnico magnet and provided new insights into aspects of domain wall pinning.[65] Other studies highlighted promising positive correlations between the elongated

spinodal structure dimensions and the resultant coercivity, opening the door for future optimization of Alnico properties.[66]

Current theoretical studies that focus on understanding the micromagnetic character of the reversal processes in elongated nanoparticles, such as those found in Alnico, reveal an evolution of nucleation and coercive fields with the variation of the precipitate aspect ratio and with the degree of precipitate smoothness,[67] as well as the effect of packing fraction on the maximum energy product.[68]

Exchange-spring Magnets

Magnetic features of exchange-spring magnets

Following a similar materials design strategy employed for the Alnico magnets in the 20th century but using 21st-century tools and new understanding to engineer magnetism at the nanoscale, research on magnetic nanocomposites represents one of the most promising pathways for realization of next-generation permanent magnets.

As previously stated, the largest possible maximum energy product of a given magnetic material with large coercivity ($H_c > M_S/2$) is determined by the intrinsic saturation magnetization:

$$(BH)_{max} \leq \frac{1}{4} \mu_0 M_S^2 \quad \text{Eq. [21]}$$

However, most high-coercivity permanent magnetic materials typically do not show very large saturation magnetization values (typically around $M_S \sim 1.0$ - 1.5 T). In the early 1990's, Kneller and Hawig,[69] and subsequently Skomski and Coey,[40] revisited early experimental work by Coehorn *et al.*[70] to indicate that combination, at the nanoscale, of high-magnetization soft ferromagnetic phase with a high-coercivity hard ferromagnetic phase to create a magnetic composite material could result in a much improved $(BH)_{max}$. This nanocomposite magnet is also known as "exchange-spring" magnet due to the largely reversible —"springy" — magnetic interaction that takes place between the magnetic components under the application and removal of an applied magnetic field. In the ideal case, the major demagnetization curve of an exchange spring magnet is characteristic of a single magnetic phase, despite the existence of two phases with very different magnetic features (Fig. 7.6). The interphase magnetic exchange coupling yields a composite system that benefits from the best attributes of the constituent phases: the magnetically hard phase furnishes high anisotropy and accompanying high coercive fields, while the magnetically soft phase donates a large saturation magnetization.

The proposed models for an ideal exchange-spring magnet microstructure employ the critical dimensions of the constituent phases to achieve the most effective coupling. In particular, the nanoscopic dimensions of the soft phase, d_{max}^s , should be on the order of twice the estimated domain wall thickness of the hard magnetic phase, δ_B^h , *i.e.*, $d_{max}^s \leq 2\delta_B^h$. [71] In this manner, nucleation of reversed domains and domain wall formation in the soft regions of the magnet are impeded, preserving a high coercivity. Thus the characteristic magnetic correlation length controls the magnetic behavior in nanocomposite magnets.

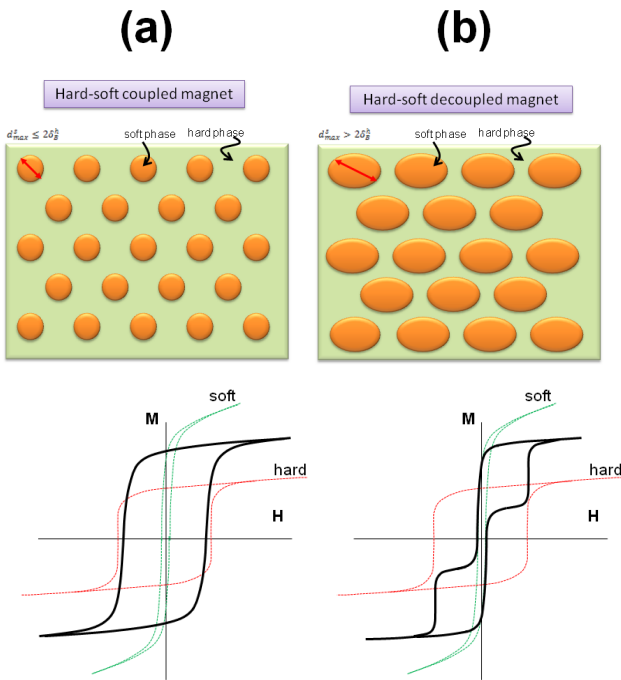


FIGURE 7.6

Schematic configuration of two hard-soft magnetic composites, with variable dimensions of the soft inclusions, (a) $d_{\max}^s \leq 2\delta_0^h$ and (b) $d_{\max}^s > 2\delta_0^h$, respectively. Illustration describing magnetization loops for exchange coupled and exchange decoupled hard-soft magnetic phases

Theoretical considerations of the nanocomposite ideal structure to realize strong interphase exchange coupling in exchange-spring magnets describe a microstructure consisting of a large quantity of well-separated soft inclusions[71,72] embedded in a hard matrix to provide high remanent magnetization values. From these studies, a refined expression of the maximum energy product that may be obtained in idealized exchange-coupled magnets is provided below:

$$(BH)_{\max} = \frac{1}{4} \mu_0 M_S^2 \left[1 - \frac{1}{2} \frac{\mu_0 (M_S - M_h) M_S}{K_h} \right] \quad \text{Eq. [22]}$$

where M_s and M_h are the magnetization values for the soft and hard phase, respectively, and K_h is the anisotropy constant of the hard phase. In this configuration, an estimated nucleation field H_N , defined as the reversed applied field that causes the domain wall enters the hard phase thus initiating magnetic reversal, is given by:

$$H_N = \frac{2(f_s K_s + f_h K_h)}{\mu_0 (f_s M_s + f_h M_h)} \quad \text{Eq. [23]}$$

where f_s and f_h are the fraction volumes of the soft and hard phases, respectively, and K_s is the anisotropy constant of the soft phase (the rest of parameters where defined previously). Within this scenario, with optimized proportions, arrangements and dimensions of the hard and soft phases, the energy product of these exchange-coupled nanocomposites could surpass those of

single-phase magnets.[40] However, the technical magnetic properties of bulk nanocomposites are not yet close to their theoretical predictions due to unresolved technical issues of phase purity, interphase interfacial condition, uniformity and crystallographic alignment.

Recent exchange-spring magnet developments

In addition to their projected superior technical magnetic performance, exchange-coupled nanocomposite magnets also represent a viable strategy to create high energy-product magnets with reduced rare-earth content. Realization of idealized $\text{Nd}_2\text{Fe}_{14}\text{B}/\alpha\text{-Fe}$ exchange-spring magnets, with a high degree of crystallographic alignment, would achieve maximum energy products up to three times that of commercial Neo magnets, with a better corrosion resistance and a lower cost.[2] Investigations on multicomponent model-system thin films and multilayers have provided much insight and benchmarking for the relevant parameters and phase dimensions necessary for robust exchange coupling.[73] Bulk synthesis of high-performing idealized nanocomposite magnets consisting of a rare-earth-based hard magnetic phase and soft $\alpha\text{-Fe}$ requires homogeneous dispersion of Fe clusters with a uniform grain size scale below 10 nm embedded in a RE-TM hard magnetic matrix for successful realization of a hard-soft composite magnet.[74] Isotropic bulk magnets can be achieved;[75,76] the challenge is making anisotropic and aligned nanocomposite, to increase B_R .

Some recent investigations have been carried on thin films and multilayers, an ideal playground for nanoscopic manipulation of the microstructure and basic research testing.[77] As an example, promising results with extraordinary values of maximum energy product close to 500 kJ/m^3 (around $\sim 60 \text{ MGOe}$), were obtained in NdFeB/FeCo composite multilayer films, in which a Ta spacer (1-2 nm) between the hard and soft phases was utilized in order to prevent from alloying between the hard and the soft phases.[78]

The implicit requirement of creating a bulk nanostructured material demands non-equilibrium synthesis techniques such as melt-spinning or mechanical alloying,[15] although it is typically challenging to control the phase proportions and microstructure to the nanoscale.[79] One of the first examples of successful fabrication of an exchange spring permanent magnet was achieved in the FePt system via the creation of an exchange-coupled nanocomposite consisting of equiatomic FePt and Fe_3Pt that was fabricated using self-assembly of nanoparticles.[80] Very large $(BH)_{max}$ values in the range of 160 kJ/m^3 (20 MGOe) were obtained in this manner, a 50% increase of the maximum energy product characteristic of the FePt hard magnet. Successful achievement of the appropriate exchange-spring microstructure will likely require the development of novel synthesis and processing routes; one recent example is an exchange-coupled $\alpha\text{-Fe/Sm}_2(\text{Fe,Si})_{17}\text{C}_x$ nanocomposite, with grain sizes below 10 nm, that was synthesized using high pressure annealing procedures.[81]

It is possible to synthesize hard-soft magnetic nanocomposites that employ rare-earth-free and platinum-free compounds as the hard magnetic phase. Potential use of small nanoparticles as building blocks for the controlled fabrication of hard nanocomposite magnets, is under exploration, with the aim of ensuring a more effective exchange coupling, alignment of the particle easy axes, etc... As a recent example, large energy products, up to $(BH)_{max}=132 \text{ kJ/m}^3$ (16.6 MGOe), have been obtained in aligned $\text{Zr}_2\text{Co}_{11}$ nanoparticles, prepared by cluster gun magnetron sputtering, with increasing values of maximum energy product when implemented into $\text{Zr}_2\text{Co}_{11}/\text{FeCo}$ nanocomposites ($(BH)_{max}=156 \text{ kJ/m}^3$, i.e. 19.5 MGOe).[82] Promising results have also been recently reported through the synthesis of hybrid ferrite (hard) – metal (soft) composites with relatively homogeneously distributed nanoparticles. Hexaferrites possess large values of exchange

length and domain-wall width that are well suited for exchange-coupled magnets that rely upon larger dimensions of soft phase inclusions. The main challenges present in this specific system are associated with the particle size control, crystallographic alignment and phase purity.[83] Another promising rare-earth-free system that may be a candidate for an exchange-spring magnet is the exchange-coupled L1₀-type MnAl(C)/ α -FeCo nanocomposite magnet. It is anticipated that in its optimized state, this proposed rare-earth-free exchange spring magnetic system will exhibit a Curie temperature in the vicinity of 550 K, preserving good magnetic performance to 400 K, with an appreciable coercivity of $H_c \sim 200$ -300 kA/m. Future efforts directed towards improving both of these candidate systems may facilitate the successful creation of a nanocomposite that can replace the lower-end rare-earth-based permanent magnets that exhibit maximum energy products $(BH)_{max} \sim 80$ –120 kJ/m³ (10–15 MGOe) at room temperature.[84]

Exchange-biased Magnets

Magnetic features of exchange-biased magnets

An alternative strategy to realize hard magnetic nanocomposites comprised of two exchange-interacting magnetic phases is the creation of “exchange-bias” magnets. Exchange bias, whereby a ferromagnetic (FM) material is exchange-coupled to an antiferromagnetic (AF) material at the interface, produces a displacement in the hysteresis loop along the field axis. This phenomenon is attributed to the exchange interaction at the FM/AF interface that pins FM moments during the reversal process, causing an increase of H_c and M_R and providing an enhanced $(BH)_{max}$ (see Fig. 7.7). Because the magnetic exchange interaction is active over very short (Ångstrom-level) dimensions, the physical proximity and condition of the antiferromagnetic and the ferromagnetic phases are important. These requirements are met by the creation of a nanostructured composite system of phases featuring large surface-to-volume phase ratios. [85]

Exchange anisotropy was first reported by Meiklejohn and Bean in 1956 for Co/CoO core-shell particles.[86] In fact, they were the first to propose the utilization of this new source of anisotropy as a tool to enhance $(BH)_{max}$ to obtain a superior permanent magnet. [87] However, to date, applications of exchange anisotropy have been typically confined to the thin film form for the design of magnetic recording and magnetoresistive devices for information technologies.

The interphase exchange coupling present in the AF/FM exchange-bias systems may be analyzed for potential permanent magnetic response in a manner analogous to that applied to exchange spring systems.[88] These analogies start in the reversal process, recorded in the demagnetization curves. In a model bilayer exchange-spring system (FM/FM), the magnitude of the critical applied field H_N that nucleates a reverse domain in the soft phase component is approximately equal to the realized exchange field H_{ex} and is provided below:

$$H_{ex} \cong H_N \sim \frac{2K_h t_h}{\mu_0 M_s t_s} \quad \text{Eq. [24]}$$

In this expression, K_h is the anisotropy constant of the hard FM phase (much larger than that of the soft FM phase, $K_s \ll K_h$), t_h is the thickness of the hard phase ($K_h t_h$ in J/m²), t_s is the thickness of the soft phase, and M_s is the saturation magnetization of the soft phase (that we assume larger than magnetization of the hard phase, $M_h \ll M_s$).[89] As appropriate to the analogous exchange-biased bilayer system (FM/AF), the exchange field at the interface, H_{ex} , may be expressed ideally as:[90]

$$H_{ex} \approx \frac{\Delta\sigma_{ex}^{FM-AF}}{\mu_0 M_{FM} t_{FM}} \quad \text{Eq. [25]}$$

where $\Delta\sigma_{ex}^{FM-AF}$ (in J/m^2) is the interfacial energy density, M_{FM} is the saturation magnetization of the ferromagnetic phase and t_{FM} is the thickness of the FM film. The condition for exchange bias observation is $K_{AF} t_{AF} \geq \Delta\sigma_{ex}^{FM-AF}$, where K_{AF} is the exchange anisotropy of the AF phase; otherwise, only coercivity enhancement, without an asymmetric field axis shift, would be observed. This provides a condition for the establishment of exchange bias and sets a minimum value for the anisotropy of the AF phase:[91]

$$K_{AF} \geq H_{ex} M_{FM} \left(\frac{t_{FM}}{t_{AF}} \right) \quad \text{Eq. [26]}$$

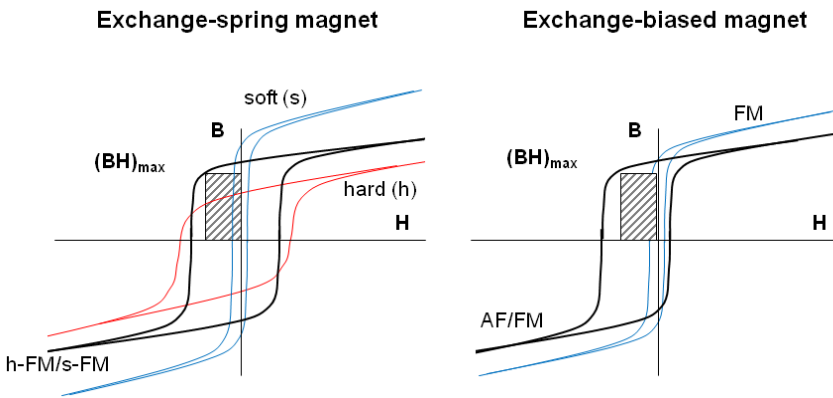


FIGURE 7.7

Illustrative picture of the effects of hard-soft magnetic exchange coupling and FM/AF exchange coupling on the maximum energy product of a magnetic nanocomposite material [reprinted with permission from Ref. 2. Copyright 2013 Springer].

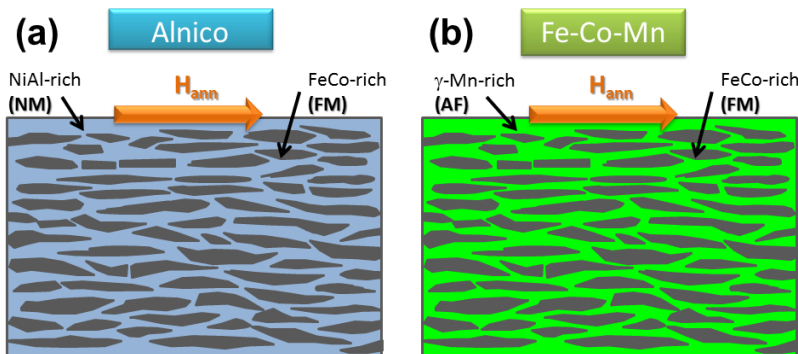
Optimization of the exchange-bias system conditions and geometry (the morphology, interfacial conditions, relative crystallographic alignment and volume contributions of FM and the AF phases) may be determined from knowledge of the critical dimensions of the AF phase. As an example, work by Mauri confirms that the exchange bias field H_{ex} characterizing a FM/AF bilayer film system, with FeMn as the AF phase, does not increase when the AF layer exceeds a certain critical thickness, t_{cr} (in this case, for FeMn $t_{cr} \approx 5$ nm).[91] In general, the exact value of the critical AF phase dimension t_{cr} depends on the specifics of the given FM/AF system; factors such as microstructure, interfacial disorder, and the transition temperature T_N (specifically, the magnetic blocking temperature of the AF phase) all influence the response.[90] This central idea of a critical phase dimension may also be applied to design of bulk exchange-biased nanocomposite systems. In all these cases it is desirable to employ theoretical approaches to provide insight into optimized geometrical parameters. All these issues evidence the importance of understanding structure-magnetic property relationships at the atomic scale and the nanoscale, engineering exchange interaction for technological use.

Recent exchange-biased magnet developments

Systems exhibiting exchange bias have been studied extensively in recent years, particularly in thin film form where the interface between the two phases is easier to control and characterize. Additionally, exchange bias phenomena are increasingly incorporated into technological applications. However, to date exchange anisotropy has not been widely investigated in magnetic materials in bulk form. A few authors in the present century have reported on exchange-bias mechanism as an underlying source of coercivity and remanence enhancement for nanocomposite magnetic materials.[92,93] Several FM/AF composite systems of FM phases combined with a variety of AF materials (NiO, MnO, CoO, FeS) synthesized by ball milling were studied; these systems were reported to display enhanced coercivity and squareness ratio at room temperature. [94,95]

However, the potential of these systems as commercial exchange-biased magnets is limited due to the significant reduction of magnetization due to the AF phase inclusion. Additionally, there are not many suitable antiferromagnetic materials that possess Néel temperatures, T_N , above room temperature as well as a sufficiently large magnetocrystalline anisotropy K_{AF} to effectively stabilize the spins in the ferromagnetic phase against magnetic reversal. The IrMn compound is one of the few high- T_N AF materials that exhibit large magnetocrystalline anisotropy at room temperature, by virtue of a large spin-orbit coupling contribution. However, while the properties of IrMn in an exchange-biased system are indeed favorable, the high cost of utilizing iridium as major constituent makes this compound unsuitable for development of bulk permanent magnets.

Nevertheless, other antiferromagnetic Mn-based alloys may be potential components of exchange-biased magnets. One advantage of these Mn-based alloys is that it is possible to tune the antiferromagnetic characteristics, such as the antiferromagnetic anisotropy constant K_{AF} or the Néel temperature T_N , through modification of the Mn concentration.[96,97] The existence of room-temperature exchange anisotropy, manifested as displaced hysteresis loops that provide enhanced coercivity, has been detected in systems containing antiferromagnetic alloys with Néel temperatures $T_N \geq 300$ K, such as Cu-Mn ($T_N \in [250, 400]$ K for Mn content ≥ 70 at.%), or Fe-Mn ($T_N \in [250, 500]$ K, variable with Mn content).[97] Weak exchange bias was obtained in a rapidly-solidified $(\text{Fe}_{65}\text{Co}_{35})_{100-x}(\text{AuMn})_x$ composite.[98] Non-equilibrium processing, such as melt-spinning or mechanical milling, is necessary for preparation of exchange-biased bulk nanocomposite systems, with capability to yield metastable phases and alloys containing increased concentrations of Mn.

**FIGURE 7.8**

Tentative illustrations describing the microstructure of (a) anisotropic Alnico; (b) FM/AF hard magnetic Fe-Co-Mn nanocomposite [reprinted with permission from Ref. [100]. (Copyright 2014 AIP Publishing LLC.)

Future efforts to combine nanoscaled antiferromagnetic phases with ferromagnetic phases such as Fe or FeCo are anticipated to exhibit an enhanced energy product to yield exchange-biased permanent magnets. Very recently, it has been proposed that utilization of AF cap layers can provide magnetic hardening of FM nanorods (Fe, Co) for hard magnetic applications, aimed to preserve the high saturation and remanence of the FM rods while attaining also large coercivities. Theoretical results suggest that the main contribution to the higher coercivity in FM nanorods with AF caps is the suppression of nucleation centers at the tips.[99] Another recent proof-of-concept example is found in Mn-based AF/FM nanocomposite formed from a rapidly-solidified nanostructured Fe-Co-Mn precursor alloy that consists of phase-separated α -FeCo (FM)/ γ -Mn-rich (AF) components.[100] This two-phase architecture was inspired by the microstructure of Alnico, which is comprised of FM FeCo-rich clusters in non-magnetic NiAl-rich matrix formed by spinodal decomposition through carefully controlled annealing. In the exchange-biased configuration, the non-magnetic NiAl layers separating the FeCo precipitates can be replaced by an antiferromagnetic Mn-rich phase (Figure 7.8). In this manner the AF phase will provide an additional source of anisotropy (exchange anisotropy) to enhance the coercivity and improve the permanent magnetic properties. Preliminary experimental results obtained from nanostructured Fe-Co-Mn alloy confirm the existence of exchange coupling at low temperature, as well as an supplemented room-temperature coercivity ($H_c \approx 350$ Oe) that is significantly larger than coercivity attributed to solely to the α -FeCo phase. Elongation of the FM precipitates by field-assisted annealing is anticipated to enhance shape anisotropy (as it does in Alnico) and provide for an appreciable energy product.

Concluding remarks

This chapter has presented an overview of existing and new pathways explored for development of the next generation of permanent magnets. Through directed design and exploitation of the fundamental properties of magnetic materials (*i.e.* intrinsic properties such as magnetization, exchange and anisotropy, and extrinsic properties such as remanence, coercivity and maximum energy product), promising results are widening the list of materials that might be included in the “magnet pool” for advanced application. In many cases, control and tailoring of the magnetic

performance is achieved through nanostructuring and control of the structural and compositional attributes at the nanoscale. These achievements are facilitated by new tools and techniques for fabrication and analysis that now available to researchers.

References

1. Skomski R. and Coey J.M.D., Permanent Magnetism; Bristol: Institute of Physics Publishing; 1999.
2. Lewis L. H. and Jiménez-Villacorta F., Metall. Mater. Trans. A 2013; 44 (Suppl.) 2-20.
3. USGS Mineral resources program, <http://minerals.usgs.gov/>
4. http://www.arnoldmagnetics.com/Calculating_Permeance_Coefficient.aspx
5. Gutfleisch O., Willard M.A., Brück E., Chen C.H., Sankar S.G. and Liu J.P, Adv. Mater. 2011; 23, 821.
6. Kittel C., Introduction to Solid State Physics; New York: John Wiley and Sons; 2005
7. Cullity B.D. and Graham C.D., Introduction to Magnetic Materials, John Wiley & Sons, Inc., Hoboken, New Jersey
8. Fischer R., Schrefl T., Kronmüller H. and Fidler J., J. Magn. Magn. Mater. 1996; 153, 35.
9. Stoner E. C. and Wohlfarth E. P., Phil. Trans. R. Soc. London A 1948; 240, 599.
10. Brown W F., Rev. Mod. Phys. 1945; 17, 15.
11. Aharoni A., Rev. Mod. Phys. 1962; 34, 227.
12. Kronmüller H., J. Magn. Magn. Mater. 1978; 7, 341.
13. Kronmüller H., Phys. Stat. Sol. B 1987; 144, 385.
14. Coey J.M.D., Magnetism and Magnetic Materials, Cambridge University Press, 2010.
15. Hadjipanayis G.C., J. Magn. Magn. Mater. 1999; 200, 373.
16. Livingston J. D., and Martin D. L., J. Appl. Phys. 1977; 48, 1350.
17. Kharel P., Skomski R., Kirby R.D. and Sellmyer D.J., J. Appl. Phys. 2010; 107, 09E303.
18. Burkert T., Nordström L., Eriksson O., and Heinonen O., Phys. Rev. Lett. 2003; 93, 027203.
19. Balamurugan B., Sellmyer D.J., Hadjipanayis G.C., and Skomski R., Scripta Mater. 2012; 67, 542-547.
20. Balamurugan B., Das B., Zhang W.Y., Skomski R. and Sellmyer D.J., J. Phys.: Condens. Matter 2014; 26, 064204.
21. Balasubramanian B., Das B., Shah V.R., Skomski R., Li X.Z. and Sellmyer D.J., Appl. Phys. Lett. 2012; 101, 122407.
22. Harris V.G., Chen Y., Yang A., Yoon S., Chen Z., Geiler A.L., Gao J., Chinnasamy C.N., Lewis L.H., Vittoria C., Carpenter E.E., Carroll K.J., Goswami R., Willard M.A., Kurihara L., Gjoka M and Kalogirou O., J. Phys. D: Appl. Phys. 2010; 43 165003.
23. Fazakas E., Varga L.K., Mazaleyra F., J. Alloy. Compd. 2007; 434-435, 611-613.
24. Kim Y.J., Perepezko J.H., J. Appl. Phys. 1992; 71, 676.
25. Jiménez-Villacorta F., Marion J.L., Sepehrifar T., Daniil M., Willard M.A. and Lewis L.H., Appl. Phys. Lett. 2012; 100, 112408.
26. Jiménez-Villacorta F., Marion J. L., Oldham J.T., Daniil M., Willard M. A. and Lewis L.H., Metals, 2014; 4, 8.
27. Zeng Q., Baker I., Cui J.B., Yan Z.C., J. Magn. Magn. Mater. 2007; 308, 214.
28. Croat J.J., Herbst J.F., Lee R.W., Pinkerton F.E., J. Appl. Phys. 1984; 55, 2078.
29. Rama Rao N.V., Gabay A.M., Li W.F. and Hadjipanayis G.C., J. Phys. D: Appl. Phys. 2013; 46, 265001.

30. Gutfleisch O., Bollero A., Handstein A., Hinz D., Kirchner A., Yan A., Muller K.-H., Schultz L., *J. Magn. Magn. Mater.* 2002; 242–245, 1277–1283.
31. Shen X.Q., Liu M.Q., Song F.Z. and Meng X.F., *J. Sol-Gel Sci. Technol.* 2010; 53, 448.
32. Gu F.M., Pan W.W., Liu Q.F. and Wang J.B., *J. Phys. D: Appl. Phys.* 2013; 46, 445003.
33. Went J., Rathenau G.W., Gorter E.W., and van Oosterhout G.W., *Philips Tech. Rev.*, 1952; 13, 194.
34. Strnat K., Hoffer G., Olson J., Ostertag W., and Becker J.J., *J. Appl. Phys.* 1967; 38, 1001.
35. Kumar K., *J. Appl. Phys.* 1988; 63, R13.
36. K.H.J. Buschow: *Magnetism and Processing of Permanent Magnet Materials*, Handbook of Magnetic Materials, vol. 10, Atlanta, GA, ed., Elsevier Science B.V., 1997.
37. Sagawa M., Fujimura S., Yamamoto H., Matsuura Y., and Hiraga K., *IEEE Trans. Magn.* 1984; 20, 1584.
38. Herbst J.F., *Rev. Mod. Phys.* 1991; 63, 81.
39. Sugimoto S., *J. Phys. D: Appl. Phys.* 2011; 44, 064001.
40. Skomski R. and Coey J.M.D., *Phys. Rev. B* 1993; 48, 15812–15816.
41. Gutfleisch O., *J. Phys. D: Appl. Phys.* 2000; 33, R157-R172.
42. Poudyal N. and Liu J.P., *J. Phys. D: Appl. Phys.* 2013; 46, 043001.
43. Bran C., Ivanov Y.P., Garcia J. del Real R.P., Prida V.M. Chubykalo-Fesenko O. and Vazquez M., *J. Appl. Phys.* 2013; 114, 043908.
44. Akdogan N.G.; Hadjipanayis G.C. and Sellmyer D.J., *J. Appl. Phys.* 2009; 105, 07A710.
45. Yue M., Wang Y.P., Poudyal N., Rong C.B. and Liu J.P., *J. Appl. Phys.* 2009; 105, 07A708.
46. Lewis L. H. and Crew D.C., *Mat. Res. Soc. Symp. Proc.* 2002; 703, U2.8.
47. Manchanda P., Kumar P., Kashyap A., Lucis M.J., Shield J.E., Mubarak A., Goldstein J.I., Constantinides S., Barmak K., Lewis L.H., Sellmyer D.J., and Skomski R., *IEEE Trans. Magn.* 2013; 49, 5194.
48. Yang J.B., Yang Y.B., Chen X.G., Ma X. B., Han J. Z., Yang Y.C., Guo S., Yan A.R., Huang Q.Z., Wu M.M. and Chen D.F., *Appl. Phys. Lett.* 2011; 99, 082505.
49. Kersten M., *Phys. Z.* 1943; 44, 63.
50. Mishima T., *Br. Patent Spec.* 378 478, 392 658 (1931); Mishima T.: *Ohm*, 1932; 19, 353.
51. <http://www.arnoldmagnetics.com/Alnico.aspx>
52. U.S. Department of Energy: “2011 Critical Materials Strategy,” December, 2011.
53. Yu C., Chau K.T., and Jiang J.Z., *J. Appl. Phys.* 2009; 105, 07F114.
54. *Springer Handbook of condensed matter and materials data*, Vol. 1, by W. Martienssen and H. Warlimont, Springer Berlin, 2005
55. Geisler A.H., *Rev. Mod. Phys.* 1953; 25, 316.
56. <http://www.duramag.com>
57. Iwama Y. and Takeuchi M., *Trans JIM* 1974; 15, 371.
58. Kittel C., Nesbitt E.A. and Shockley W., *Phys. Rev.* 1950; 77, 839.
59. De Vos K.J., *Magnetism and Metallurgy*, Volume 2, London, Academic Press; 1969.
60. Cahn J.W., *J. Appl. Phys.* 1963; 34, 3581.
61. Luborsky F.E., *J. Appl. Phys.* 1966; 37, 1091.
62. *Standard Specifications for Permanent Magnet Materials (MMPA Standard No. 0100-00)*, Magnetic Materials Producers Association, Chicago Illinois.
63. Luborsky F.E., Mendelsohn L.I. and Paine T.O., *J. Appl. Phys.* 1957; 28, 344.
64. Xing Q., Miller M.K., Zhou L., Dillon H.M., McCallum R.W., Anderson I. E., Constantinides S., and Kramer M. J., *IEEE Trans. Magn.* 2013; 49, 3314.

65. Palasyuk A., Blomberg E., Prozorov R., Yue L., McCallum R.W., Anderson I. E., and Constantinides S., *JOM* 2013; 65, 862.
66. Hadjipanayis G.C., Frincu B., Löwe K., Hu X., Gutfleisch O., *Bulletin of the American Physical Society* 2014; 59 (1), D54.00004.
67. Bance S., Fischbacher J., Schrefl T., Zins I., Rieger G., Cassignol C., *J. Magn. Magn. Mater.* 2014; 363 121–124.
68. Skomski R., Liu Y., Shield J.E., Hadjipanayis G.C. and Sellmyer D.J., *J. Appl. Phys.* 2010, 107, 09A739.
69. Kneller E., Hawig R., *IEEE Trans. Magn.* 1991; 27, 3588.
70. Coehoorn R., de Mooij D.B., Duchateau J.P.W.B. and Buschow K.H.J., *J. de Phys.* 1988; 49 C8-669.
71. Fischer R., Leineweber T., and Kronmüller H., *Phys. Rev. B* 1998; 57, 10723.
72. Arcas J., Hernando A., Barandiarán J. M., Prados C., Vázquez M., Marín P., Neuweiler A., *Phys. Rev. B* 1998; 58, 5193.
73. Liu J.P., Skomski R., Liu Y., Sellmyer D.J., *J. Appl. Phys.* 2000; 87, 6740.
74. Hiroswawa S., Kanekiyo H. and Uehara M., *J. Appl. Phys.* 1993; 73, 6488.
75. Lewis L.H., Moodenbaugh A.R., Welch D.O. and Panchanathan V., *J. Phys. D: Appl. Phys.* 2001; 34, 744–751.
76. Rong C.B., Zhang Y., Poudyal N., Xiong X.Y., Kramer M.J. and Liu J.P., *Appl. Phys. Lett.* 2010; 96, 102513.
77. Liu J.P., Skomski R., Liu Y., Sellmyer D.J., *J. Appl. Phys.* 2000; 87, 6740.
78. Cui W.-B., Takahashi Y.K., Hono K., *Adv. Mater.* 2012; 24, 6530.
79. Li Z.B., Shen B.G., Niu E. and Sun J.R., *Appl. Phys. Lett.* 2013; 103, 062405.
80. Zeng H., Li J., Liu J.P., Wang Z.L. and Sun S., *Nature* 2002; 420, 395.
81. Zhang X., Zhang J., and Wang W., *Adv. Mater.* 2000; 12, 1441.
82. Balasubramanian B., Das B., Skomski R., Zhang W.Y. and Sellmyer D.J., *Adv. Mater.* 2013; 25, 6090.
83. <http://nanopyme-project.eu/>
84. McCallum R.W., Lewis L.H., Skomski R., Kramer M.J. and Anderson I.E., *Ann. Rev. Mater. Res.* 2014; 44, 10.1-10-27.
85. Nogués J., Sort J., Langlais V., Skumryev V., Suriñach S., Muñoz J.S., Baro M.D., *Phys. Rep.*, 2005; 422, 65.
86. Meiklejohn W. H. and Bean C. P., *Phys. Rev.* 1956; 102, 1413.
87. Meiklejohn W. H. and Bean C. P., *Phys. Rev.* 1957; 105, 904.
88. Jiang J. S., Inomata A., You C.-Y., Pearson J.E. and Bader S.D., *J. Appl. Phys.* 2001; 89, 6817.
89. Fullerton E.F., Jiang J.S., Bader S.D., *J. Magn. Magn. Mater.* 1999; 200, 392.
90. Berkowitz A.E., Takano K., *J. Magn. Magn. Mater.* 1999; 200, 552.
91. Mauri D., Siegmann H.C., Bagus P.S., Kay E., *J. Appl. Phys.* 1987; 62, 304.
92. Skumryev V., Stoyanov S., Zhang Y., Hadjipanayis G., Givord D. and Nogués J., *Nature* 2003; 423, 850-853
93. Jiménez-Villacorta F. and Prieto C., *J. Phys.: Condens. Matter*, 2008; 20, 085216.
94. Mishra S. R., Dubenko I., Losby J., Roy S., Ali N. and Marasinghe K., *IEEE Trans. Magn.* 2004; 40, 2716.
95. Sort J., Nogués J., Amils X., Suriñach S., Muñoz J.S., and Baró M.D., *Appl. Phys. Lett.* 1999; 75, 3177.

96. Jiménez-Villacorta F., Puente-Orench I., Rodríguez-Carvajal J. and Lewis L. H., (*in preparation*).
97. The Landolt-Bornstein database:
http://www.springermaterials.com/navigation/navigation.do?m=l_1_278610_
98. Lewis L.H., Harland C. L., McCallum R.W., Kramer M. J. and Dennis K.W., *J. Appl. Phys.* 2006; 99, 08E908.
99. Toson P., Asali A., Fidler J., Salikhov R., Spasova M., Farle M., presented at the Intermag 2014 Conference, Dresden, Germany.
100. Jiménez-Villacorta F., McDonald I., Heiman D. and Lewis L.H., *J. Appl. Phys.* 2014; 115, 17A729.